Faraday Discussions

Cite this: DOI: 10.1039/d6fd00003g

PAPER

View Article Online
View Journal

Effect of hybrid field coupling in nanostructured surfaces on anisotropic signal detection in nanoscale infrared spectroscopic imaging methods

Ayona James,[ab] Maryam Ali,[ab] Zekai Ye,[b] Phan Thi Yen Nhi,[ab] Sharon Xavi,[ac] Mashiat Huq,[c] Sajib Barua,[bc] Meng Luo,[c] Yisak Tsegazab,[ab] Anna Elmanova,[ab] Robin Schneider,[b] Olga Ustimenko,[d] Sarmiza-Elena Stanca,[b] Marco Diegel,[b] Andrea Dellith,[b] Uwe Hübner,[b] Christoph Krafft,[ab] Jasmin Finkelmeyer,[b] Maximilian Hupfer,[ab] Kalina Peneva,[def] Matthias Zeisberger,[b] Christin David,[gh] Martin Presselt[ab] and Daniela Täuber*[ab]

Received 9th January 2026, Accepted 27th January 2026

DOI: 10.1039/d6fd00003g

Anisotropic intensity distributions on nanostructured surfaces and polarization-sensitive spectra have been observed in a number of nanoscale infrared spectroscopic imaging methods, including nano-FTIR [Bakir *et al.*, *Molecules*, 2020, **25**, 4295], photothermal induced resonance (PTIR) [Waeytens *et al.*, *Analyst*, 2021, **146**, 132], tapping AFM-IR [Hondl *et al.*, *ACS Meas. Sci. Au*, 2025, **5**, 469; Luo *et al.*, *Appl. Phys. Lett.*, 2022, **121**, 233301], infrared photoinduced force microscopy (IR-PiFM, PiF-IR) [Anindo *et al.*, *J. Phys. Chem. C*, 2025, **129**, 4517; Shcherbakov *et al.*, *Rev. Methods Primers*, 2025, **5**, 34; Ali *et al.*, *Anal. Chem.*, 2025, **97**, 23914] and peak force infrared microscopy (PFIR) [Xie *et al.*, *J. Phys. Chem. C*, 2022, **126**, 8393; Anindo *et al.*, *J. Phys. Chem. C*, 2025, **129**, 4517]. A recent work combining modeling and experiment demonstrated that the hybrid field coupling of the IR illumination E_0 with a polymer nanosphere and a metallic AFM probe is nearly as strong as the plasmonic coupling in case of a gold nanosphere

---

[a] *Institute of Physical Chemistry (IPC), Friedrich Schiller University Jena, 07743 Jena, Germany. E-mail: dantaube@gmx.de*

[b] *Leibniz Institute of Photonic Technology (LIPHT), 07745 Jena, Germany*

[c] *Abbe School of Photonics, Friedrich Schiller University Jena, 07745 Jena, Germany*

[d] *Institute of Organic and Macromolecular Chemistry (IOMC), Friedrich Schiller University Jena, 07743 Jena, Germany*

[e] *Jena Center of Soft Matter (JCSM), Friedrich Schiller University Jena, 07743 Jena, Germany*

[f] *Center for Energy and Environmental Chemistry Jena (CEEC Jena), Friedrich Schiller University Jena, 07743 Jena, Germany*

[g] *Institute of Condensed Matter Theory and Solid State Optics (IFTO), Friedrich Schiller University Jena, 07743 Jena, Germany*

[h] *University of Applied Sciences Landshut, 84036 Landshut, Germany*

[Anindo *et al.*, *J. Phys. Chem. C*, 2025, **129**, 4517]. For p-polarized illumination, this results in enhanced IR absorption on the surface perpendicular to the propagation of E_0 which can explain the observed anisotropic intensity distribution. An additional anisotropy may be introduced by aligned surface molecules with oriented vibrational transition moments [Bakir *et al.*, *Molecules*, 2020, **25**, 4295; Luo *et al.*, *Appl. Phys. Lett.*, 2022, **121**, 233301]. PiF-IR is strongly surface sensitive combining an unprecedented spatial resolution <5 nm with high spectral resolution [Shcherbakov *et al.*, *Rev Methods Primers*, 2025, **5**, 34; Ali *et al.*, *Anal. Chem.*, 2025, **97**, 23914], which allows, for example, the visualization of nanoscale chemical variation on the surface of bacteria cells affected by antimicrobial interaction [Ali *et al.*, *Anal. Chem.*, 2025, **97**, 23914]. We compare PiF-IR hyperspectra of aligned perylene Langmuir–Blodgett monolayers on nanostructured and planar gold substrates and use quantum chemical calculations of the oriented vibrational oscillators to interpret the observations.

Introduction

The emerging field of nanoscale infrared spectroscopic imaging (NanIR) methods[1–3] has the potential to revolutionize our understanding of chemical compositions and molecular arrangement in life and material sciences in a way similar to the ground-breaking insights gained from the emergence of fluorescence microscopy. NanIR methods can bridge the gap between high-resolution structural imaging in electron and atomic force microscopy (AFM) and chemical imaging in conventional far-field infrared (IR) spectroscopy by overcoming the limitations of optical diffraction in far-field IR spectroscopic imaging and provide complementary information to tip enhanced Raman scattering (TERS).[4] By exploiting near-field enhanced IR absorption mediated by metal nanostructures, NanIR methods provide access to chemical characterization on the scale of a few nanometers, for example, of antibiotic interaction on the surface of individual bacteria cells.[5] The highly localized and non-linear absorption is influenced by geometrical parameters in the setup, such as bottom-up and top-down illumination,[6] the orientation of the linearly polarized IR illumination[6–9] and the geometry of the induced near-field.[10] On nanostructured samples, such effects result in anisotropic signal detection, which has been reported on a variety of nanoparticles employing different NanIR methods.[6,10–12] A better understanding of these effects will result in an improved interpretation of measured signals on nanostructured materials yielding valuable complementary information over a large range of applications.

In general, NanIR methods can be grouped by their approach for signal detection: in surface-enhanced infrared absorption (SEIRA) spectroscopy[13,14] and infrared scattering scanning optical near-field microscopy (IR s-SNOM and nano-FTIR)[15,16,55] near-field enhanced absorption is combined with optical far-field detection. In contrast, the so-called AFM-IR methods[2] combine IR absorption enhanced by a sharp metallic tip with mechanical detection *via* atomic force microscopy (AFM). Thereby, peak force infrared microscopy (PFIR)[2,11] and photothermal induced resonance (PTIR)[6,17] and its refined methods: resonantly enhanced infrared nanospectroscopy (REINS)[18] and tapping AFM-IR[19,20] detect photoinduced thermal expansion upon IR illumination, whereas, in IR photoinduced force microscopy (IR-PiFM or PiF-IR) the photoinduced tip-sample interaction force in the attractive regime is acquired.[10,12,21,22] PiF-IR provides access to the chemical characterization of the molecular arrangement on surfaces with a spatial resolution of less than 5 nm.[5,23,24] This sharp tool can be used to explore optical parameters contributing to field effects and to find tiny contributions from materials (contaminations)[25] and impacts from approaches in handling the measurements.

Several studies have evaluated hybrid field coupling in NanIR methods for planar layered structures, for example, Jahng *et al.* calculated the photoinduced force obtained in PiF-IR for a thin layer of polystyrene on a Si substrate and compared their theoretical results with experimental results.[26] Pascual Robledo *et al.* used electrostatic numerical calculations of infrared near-field spectra in isotropically and anisotropically absorbing dielectric layers on planar CaF_2 and Au substrates, which did not include far-field reflections on the substrate. They found that for very thin layers, the proximity of the Au substrate forces the field lines to align vertically, preventing coupling to in-plane molecular vibrations.[55] Xie *et al.* applied PFIR and visible peak force microscopy to organo-metal-halide perovsike nanostructures[11] and compared their experimental results with near-field modeling. The studied materials show isotropic absorption of the organic compound in the mid-IR and anisotropic visible absorption related to the crystal structure.[27] Anindo *et al.* modeled the hybrid photo-induced near-field between a Pt-tip and an isotropically absorbing polymer nanoparticle and compared their results with experimentally obtained results using PiF-IR.[12] Waeytens *et al.* compared bottom-up and top-down PTIR illumination probing amyloid fibril structures with different polarization states of the incoming light field and varying the coating material of the tip both experimentally and with a simplified theoretical approach.[6] Their theoretical model assumes a constant electric incident field and a quasistatic optical response of the involved nanoparticles: a cylindrical fibril and a spherical Au tip. They showed that because of the tip curvature, the components of the electric field change directionality in the vicinity of the tip and can add to the enhancement of absorption in p-polarization while they reduce the field inside the probe for s-polarization,[6] which is in agreement with theoretical considerations of tip-enhanced fields reported by other research groups.[12,26] In amyloid fibrils, proteins organize in a highly oriented β-sheet structure. Thereby, the transition dipole moment μ_β of the β-sheet absorption at 1620 cm^{-1} is perpendicular to the fibril's long axis.[6] For a single fibril with μ_β aligned parallel to the s-polarization, Waeytens *et al.* found an enhanced signal in the bottom-up illumination for s-polarized light, while the signal in p-polarization could hardly be discriminated from the noise.[6] Probing ensembles of arbitrarily oriented amyloid fibrils assembled from three different proteins, they found varying spectral signatures between the three different samples, which can be explained by different percentages of amino acids involved in the formation of β-sheets in those proteins. For the two proteins that involve a high percentage of amino acids in the formation of β-sheets, PTIR spectra obtained under bottom-up illumination showed a high intensity in the β-sheet absorption band, while the intensity of this band was strongly reduced under top-down illumination. In both configurations, Au tips and p-polarization were used. However, for top-down illumination, this results in a higher polarization perpendicular to the sample plane than for bottom-up illumination,[6] while the in-plane components for in-plane polarization are comparable, which might contribute to the observation.

In this work, we applied high-precision PiF-IR to oriented molecular monolayers of an alkylated perylene-monoimide (PMIS-C8) on nanostructured and planar Au substrates to study the effects of anisotropic absorption in nanostructured surfaces in NanIR imaging experimentally. Asymmetric and amphiphilic perylenes[28] are ideal test systems for this purpose, because their chemical structure is well-defined, with IR-active functional groups firmly anchored to the molecular backbone. Due to their condensed aromatic systems, the number of internal rotational or torsional degrees of freedom is severely limited. The amphiphilicity of the perylenes makes them ideal for producing oriented molecular monolayers using Langmuir–Blodgett (LB) and related methods.[29] We calculated polarization-resolved IR spectra of PMIS-C8 and used them to interpret our experimental results. We further compare the experimentally obtained local PiF intensity variation on nanostructured Au to the field distribution of the photo-induced near-field on a model of the Au nanostructure simulated using a finite element method (FEM) approach.

Methods

Au substrates

Two types of Au substrates were used: (i) nanostructured Au: 100 nm Au were evaporated onto a 0.6 mm thick SiO_2 chip, resulting in nanostructured Au surfaces consisting of a dense population of ≈15 nm high and ≈50 nm wide hills and (ii) planar Au: 200 nm Au were evaporated onto a Si wafer. Subsequently, a SiO_2 chip was placed onto the Au layer. When the chip was carefully removed, the Au layer adhered to the SiO_2 exposing the smooth surface that had been formed at the interface with the Si wafer.

Perylene

The *N*-octylmonoimide of 9,10-bis([1,2] dithiole)-1,6,7,12-tetrachloroperylene (PMIS-C8) was synthesized as described previously.[29,30] For comparative infrared spectroscopy, PMIS-C8 was dissolved in CCl_4 with a concentration of (0.339 μmol mL^{-1}).

Langmuir–Blodgett (LB) films

LB films were prepared following established procedures[31–33] using a PMIS-C8 dichloromethane solution (0.1 μmol mL^{-1}) and a target surface pressure of 20 mN m^{-1}. The spread volume was 700 μL and 900 μL for nanostructured and planar Au substrates, respectively.

Film deposition for the two final samples on nanostructured Au was carried out using a KSV NIMA Langmuir and Langmuir–Blodgett trough in the education lab at the Institute of Physical Chemistry. For all other samples, a KSV 5000 Langmuir–Blodgett trough available in the Presselt lab was used. In the KSV 5000, two substrates were mounted simultaneously by attaching each to a clip in the sample holder. The barrier compression speed was set at 10 mm min^{-1}, corresponding to a compression rate of approximately 5 mN m^{-1} min^{-1}. Film formation was monitored using Brewster Angle Microscopy (BAM). In the smaller KSV NIMA, only one sample was mounted and the barrier compression speed was set at 3.5 mm min^{-1}, corresponding to the same compression rate of approximately 5 mN m^{-1} min^{-1}. In both instruments, the substrates were pulled out at a speed of 2 mm min^{-1} during deposition and the transfer of the monolayer to the Au substrates was carried out at a surface pressure of 20 mN m^{-1}.

Brewster angle microscopy (BAM)

BAM measurements were carried out using a KSV NIMA MicroBAM system (Biolin Scientific, Finland) equipped with a 659 nm laser illumination with 50 mW maximum laser power at the aperture, a microscope objective lens and a CCD detector. BAM images were recorded every 20 min on a 3580 μm wide area *in situ* during monolayer formation at the air–water interface. Exemplary BAM images of a PMIS-C8 film formed at the water surface are shown in the SI in Fig. S1.

Atomic force microscopy (AFM)

AFM height and phase images were acquired in air in tapping mode ($f_t = 197$ kHz or $f_t = 307$ kHz) on a Bruker-AFM Dimension Edge™ (BrukerAXS, Karlsruhe, Germany). 20 μm wide overviews and 5 μm wide higher resolution scans were acquired with scan resolutions of 39 nm per pixel and 9.8 nm per pixel, respectively. AFM data were processed using the following tools in Gwyddion:[34] (i) level data by mean plane subtraction, (ii) align rows using various methods (applying a 5th degree polynomial) and (iii) correct horizontal scars. Height images were additionally processed using the tool (iv) level data to make facets point upward. AFM height and phase images of pristine Au substrates and PMIS-C8 monolayer films are presented in the SI in Fig. S2 and S3, respectively.

Mid-IR photo-induced force microscopy (PiF-IR)

PiF-IR was conducted on a commercial VistaScope™ (Molecular Vista, US) equipped with a pulsed quantum cascade laser (MirCat™, Daylight Solutions, US), which was tuned in the spectral range of 800–1800 cm^{-1} and operated in side band mode.[12,22] For this, the pulse frequency f_m of the MirCat™ was tuned to match $f_m = f_2 - f_1$, where f_1 and f_2 are the first and second mechanical resonance frequencies of the PtIr-coated AFM cantilever (Point Probe Plus, Nanosensors, CH). The photo-induced force (PiF) was acquired in the side band mode at f_1, while a second login amplifier was used to record the topography at the driving frequency f_2. Due to the smaller amplitude of the oscillation at f_2, the topography contrast is more sensitive to instrument noise than the PIF contrast acquired at f_1. In several positions, height differences caused by a tilt in the sample mounting exceeded the small height difference of 10–30 nm in our samples. These topography images were processed using line averages in the fast scanning (horizontal) direction. PiF contrasts were not corrected.

The illumination power was homogenized over the spectral range by clipping the illumination intensity to manually selected percentages of peak values in previously obtained power spectra. Depending on the selected value, this resulted in an illumination power in the range of 20–40 μW with a focal spot diameter of $\approx 2\lambda$. For this procedure, power spectra are acquired in direct mode at f_1 and f_2 in air. A "side-band" power spectrum is then calculated from the obtained oscillation amplitudes at both frequencies.[7] The quality of the homogenization strongly depends on the stability of the IR beam alignment to the tip-sample region. To recover the alignment after mounting new samples, we first validated the alignment in air and then acquired new power spectra before starting data acquisition. The instrument was purged with N_2 to reduce the contributions of water vapor absorption to the acquired spectra. Nevertheless, slight variations in humidity between the acquisition of the power spectra and subsequent data acquisition may result in residual contributions of water vapor lines to the acquired spectra. Since we installed the new powerful MirCat light source in the instrument, we frequently have observed rather strong baselines that rise from lower to higher frequencies. Two examples are seen in the PiF-IR spectra in Fig. 1a and b. The cause of this rise is not yet fully known and there is a nonlinear dependence of the PiF on illumination power. Thus, we decided not to apply any math operations to remove this rise.

PiF-IR single point spectra are usually acquired on selected positions in a previously scanned sample area. Although the high-precision closed loop scanner in the instrument causes only small drifts of a few nanometers between succeeding single frequency illumination scans of the same sample area, consecutive moves to selected positions for point spectra will result in an accumulated drift on the scale of the structural variation in the nanostructured Au substrate. In hyperspectral PiF-IR scans, much higher positional accuracy is provided, enabling the comparison of spectral bands at particular sample positions. Due to the much longer acquisition time ($\approx$20 h), the instrument drift accumulates over the hyperscan, resulting in scan areas elongated in the slow scan direction compared to much faster single frequency scans (20–120 min).

PiF-IR data analysis of single frequency scans, hyperspectral scans, and spectra was conducted using the instrument software SurfaceWorks™ (Molecular Vista, US). At interesting vibrational frequencies ν, spectral channels with bandwidth ν

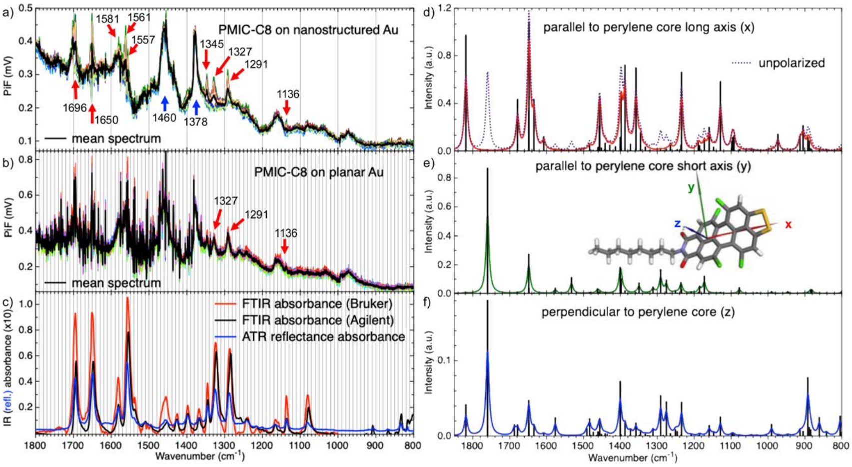

Fig. 1 Experimental and computed infrared spectra of PMIS-C8. (a and b) PiF spectra of the PMIS-C8 monolayer on nanostructured and on planar Au, respectively; red and blue arrows in (a) mark bands showing intensity variations and no variations, respectively; (c) FTIR and ATR spectra; (d and e) computed stick and line broadened IR spectra: (d) unpolarized line broadened spectrum (dotted line) and component spectra parallel to long axis (*x*) of perylene core (solid line, and stick spectrum), (e) component spectra parallel to short axis (*y*) of perylene core and (f) component spectra perpendicular (*z*) to perylene core.

$\pm$ 2 cm^{-1} were extracted from hyperspectral scans. Hierarchical Cluster Analysis (HCA) of PiF-IR hyperspectra was performed using our home-written software hyPIRana.[35] Three HCA clusters were obtained from the dendrograms. For each cluster, mean spectra (HC1, HC2 and HC3) were calculated. We applied a non-negative factorization to obtain cluster maps to study the relative contribution of each cluster in each spectrum (S) of the hyperspectral data set: $S = \alpha_1\mathrm{HC1} + \alpha_2\mathrm{HC2} + \alpha_3\mathrm{HC3}$. The resulting factor maps show relative contributions of the three components in each pixel. PiF-IR is highly sensitive to contaminants.[25] Polydimethylsilane (PDMS), a highly volatile polymer, was frequent in our lab. We used its characteristic absorption at 1262 cm^{-1} to check for sample contamination by PDMS.

Conventional infrared (IR) spectroscopy

Attenuated total reflection (ATR) spectroscopy was conducted on a commercial instrument (model 670, Agilent, US) at a spectral resolution of 2 cm^{-1}. 30 μL PMIS-C8 solution was dripped onto a ZnSe crystal. ATR spectra were acquired after evaporation of CCl_4. The spectra were calibrated from a background taken before droplet disposal and corrected for multiple reflections using the instrument software (Resolution Pro v.5.3).

Fourier transform infrared (FTIR) spectra were acquired from a dried droplet of 10 μL PMIS-C8 solution dripped on a CaF_2 window (Crystec, Berlin) at a spectral resolution of 2 cm^{-1}, 32 spectra per probe in the spectral range of 600–4000 cm^{-1} in transmission mode using two different commercial instruments: (i) a Hyperion microscope (Bruker, US) equipped with a Cassegrain 15×/NA 0.4 objective connected to a Bruker Vertex 80v spectrometer. The samples were illuminated with a silicon carbide (SiC) infrared light source and the spectra were collected with a standard FTIR detector with Mercury Cadmium Telluride (MCT) diode (D^*: $>2 \times 10^{10}$ cm $Hz^{1/2}$ W^{-1}) liquid nitrogen cooled. The measurements were performed at the source aperture of 4 mm, KBr beam splitter, collection mirror velocity 20 kHz. The spectra were recorded on a square sample spot measuring 400 μm × 400 μm. Reference for transmission mode: air. OriginPro™ was used for baseline correction. (ii) an Agilent model 670 (Agilent, US) equipped with a Cassegrain 15×/NA 0.4 objective. The spectrometer chamber was enclosed in a homebuilt box and purged by dry air to reduce the spectral contributions of water vapor. Instrument software (Resolution Pro v.5.3) was used to calibrate the FTIR spectra from a background taken on a clean substrate. Previously acquired water vapor spectra were used to remove residual water lines from the spectra.

Computation of IR spectra

Quantum chemical calculation. Quantum chemical structure optimizations along with the calculations of vibrational spectra were carried out using density functional theory (DFT) as implemented in the GPU-accelerated program TeraChem.[36–42] To account for non-covalent interactions, Grimme's D3 dispersion correction was employed for all calculations.[43,44] All geometries were optimized at the CAM-B3LYP[45] level of theory with the valence double-ζ basis set Ahlrichs-pVDZ, including polarization functions on all atoms as introduced by Ahlrichs and co-workers.[46] The optimized structures were confirmed as true minima through frequency calculations.

Post-processing and vibrational analysis. The calculated vibration data were further processed using a custom script to determine IR intensities and generate theoretical spectra.

Data extraction and coordinate system definition. The script parsed the final optimized geometries, Atomic Polar Tensors (APTs), and mass-weighted normal modes from the TeraChem output files. To establish a consistent frame of reference, the molecule was oriented into its standard orientation, placing the center of mass at the origin and aligning the Cartesian axes with the principal axes of inertia. This procedure aligns the x-axis with the long axis of the planar aromatic core, the y-axis orthogonal to the molecular plane, and the z-axis within the plane, perpendicular to the x-axis. This well-defined coordinate system served as the foundation for all subsequent vector analysis.

Calculation of Cartesian displacements and IR intensities. From the calculation output, the Atomic Polar Tensor (APT) and mass-weighted normal modes were extracted. The mass-weighted modes were subsequently converted to Cartesian displacement vectors (I) to present the true physical motion of the atoms. The transition dipole moment vector (μ) for each mode, also known as IR-transition vector, was calculated by the matrix product of the APT and the corresponding displacement vector ($\mu = \text{APT} \times I$). The total IR intensity was then derived from the squared magnitude of this vector ($\mu^2 = {\mu_x}^2 + {\mu_y}^2 + {\mu_z}^2$), and its individual components were also resolved to understand the directional character of each absorption.

Generation of theoretical IR spectra. The computed vibrational frequencies and corresponding IR intensities were used to construct discrete IR stick spectra. To simulate experimental absorption profiles, each transition was convoluted with a Lorentzian line-shape function using a full width at half maximum (FWHM) of 10.0 cm^{-1}. This yielded a broadened theoretical IR spectrum. To further examine the directional character of absorption, the squared Cartesian components of the transition dipole moment (${\mu_x}^2$, ${\mu_y}^2$, ${\mu_z}^2$) were individually convoluted using the same broadening function to generate component-resolved spectra for the x, y, and z directions.

Visualization of vibrational modes. To facilitate mode assignment, interactive 3D visualizations were created using the py3Dmol library,[47] allowing inspection of static atomic displacement vectors and dynamic animations of vibrational motions.

Modeling hybrid field coupling

In this work, the optical properties of nanostructures on substrates are simulated using the finite element method (FEM) implemented in COMSOL Multiphysics 6.3 using the wave optics module in the frequency domain. The refractive index of gold (Au) used for the modeling is taken from Olmon *et al.*[48] covering wavelengths from 3 to 25 μm well into the infrared. An Au nanostructure is placed on a 100 nm thick planar Au layer on top of a 100 nm thick SiO_2 (ref. 49) layer. Floquet periodic boundary conditions were applied to all four surrounding surfaces to simulate a periodic array of nanosized unit cells. The excitation light wave is p-polarized (TM) and incident at an angle of 60°.

The Au nanostructure has the shape of a $\cos^2(\pi x/R)$ function with radius of 25 nm and a height of 15 nm and the width of the unit cell being $2R = 50$ nm. This 2D parametric curve is then revolved around the z-axis to obtain a 3D nanostructure. A very fine mesh with elements of an average size of 2.5 nm was used on the surface of the curved structure. Further details on the simulations can be found in the SI.

Results

Intensity variations of characteristic PMIS-C8 bands in PiF-IR spectra

Single-point PiF-IR spectra acquired at various positions on a PMIC-C8 monolayer on nanostructured Au show intensity variations in several absorption bands, which are marked by red arrows in Fig. 1a. These bands are related to vibrations in the imide group (antisymmetric and symmetric C=O stretch at 1696 and 1650 cm^{-1}, respectively)[50] and the perylene core (C=C in-plane stretch at 1581 cm^{-1},[50] C=C out-of-plane stretch at 1561 & 1557 cm^{-1},[51] C=C and CN in-plane stretch at 1345 cm^{-1},[50] and CH bend at 1327 & 1291 cm^{-1} (ref. 51)). In contrast, the two strong bands appearing at 1460 and 1378 cm^{-1} (blue arrows in Fig. 1a) show no such variations above noise level. These two bands are related to CH_3 and CH_2 bending[52] in the alkyl chain. All these bands also appear in PiF-IR single-point spectra acquired at several positions on a PMIS-C8 monolayer on planar Au; see Fig. 1b. However, the spectra of this sample show strong contributions by water vapor in the spectral range between 1800 and 1350 cm^{-1}. The PiF signal obtained from the monolayer on planar Au was considerably weaker than that obtained from PMIS-C8 on nanostructured Au. We therefore had increased the illumination power from ≈20 mW to ≈40 mW, which resulted in comparable PiF intensities, in agreement with the ratio of average field intensities of photoinduced fields on planar and nanostructured Au obtained from modeling; see Table S1 in the SI. Unfortunately, the increased illumination power also increased the sensitivity of the PiF signal to contributions resulting from incomplete compensation for water vapor, resulting in noisy spectra in this spectral region. Nevertheless, the bands at 1327, 1291 and 1136 cm^{-1} related to perylene core vibrations are visible outside this noisy region; see red arrows in Fig. 1b. In contrast to the PiF spectra obtained from PMIS-C8 on nanostructured Au (Fig. 1a), all PiF spectra in this data set show similar intensities in these three bands, reporting a rather homogeneous orientation of the perylene core in the investigated positions of the PMIS-C8 monolayer on the planar Au substrate. We will discuss molecular orientation in more detail after a comparison of PiF-IR spectra with conventional IR spectra.

The vibrational bands of PMIS-C8 discussed above are also visible in conventional ATR and FTIR spectra; see Fig. 1c. Table 1 provides a comparison of band positions of the major PMIS-C8 bands for the three experimental methods, including also calculated spectra. In general, the band positions agree quite nicely for the three experimental methods. The band positions of the calculated spectra show considerable deviations from the experimental ones, in particular for the antisymmetric and symmetric carbonyl vibrations of the imide moiety, which appear in the experimental spectra at ≈1696 and ≈1650 cm^{-1}, respectively. Calculations were conducted for a single PMIS-C8 molecule assuming a polar environment, which does not fully reproduce experimental conditions. In particular, PMIS-C8 is known to form dimers in monolayer films on silver (Ag) substrates.[53] As can be seen in Fig. 1c, the band positions slightly differ between

Table 1 Vibrational bands of PMIC-C8 and their assignment to vibrations of imide (I), perylene core (P) and alkyl chain (A)

PiF-IR ($\pm$1 cm^{-1})	ATR ($\pm$1 cm^{-1})	FTIR ($\pm$1 cm^{-1})	Computed (cm^{-1})	Band assignment	$\mu\|$ to axis
1696	1696	1693	1819	C=O (I) antisym. stretch[50]	x, z
1650	1650	1648	1760	C=O (I) sym. stretch[50]	y, z
1581	1581	1581	1679	C=C (P) in-plane stretch[50]	x, z
			1648		
			1634		
1561	1558	1555	1608	C=C (P) out-of-plane stretch[51]	y, z
1557			1533		
1460	1457	1452	1456	CH$_3$ and CH$_2$ (A) bending[52]	x, z, y
	1425	1426	1401		
1378	1398	1397	1398		
1366	1367	1367	1388		
1345	1345	1344	1358	C=C, CN (P) in-plane stretch[50]	x
1327	1325	1324	1346	CH (P) bend & CC def. (A)[51]	x
			1332		x
1291	1288	1284	1291	CH$_3$ and CH$_2$ (A): H–C–H	y, z, x
			1276	twist[51] & CH (P) bend	y, z
1136	1136	1136	1129	CH (P) and CH$_2$ (A)	x, z

ATR and FTIR spectra acquired on the same instrument (Agilent spectrometer) and also between the FTIR spectra acquired on two different instruments. In addition, relative band intensities vary considerably between spectra acquired using different methods or instruments. Such variations are expected from different illumination geometries and baseline corrections, which can also explain the slight variations between band positions in conventional IR spectra and PiF-IR spectra. The cause of the rather strong baselines rising from lower to higher frequencies in PiF-IR spectra (Fig. 1a and b) is not fully understood; for details see the methods section.

A remarkable difference between the PiF-IR spectra of monolayer PMIS-C8 films and conventional IR spectra acquired on PMIS-C8 droplets on CaF$_2$ after solvent evaporation is the two strong and broad bands at 1460 and 1378 cm^{-1} in the PiF-IR spectra (blue arrows in Fig. 1a). Using quantum chemical calculations, we found several CH$_3$ and CH$_2$ bending vibrations of the alkyl chain in this spectral region; see Table 1 in agreement with literature reports.[52] In the conventional IR spectra, these bands are much weaker compared to the other bands, and several sub-bands are resolved (Fig. 1c), which seem to appear as shoulders in the broad bands in the PiF-IR spectra (Fig. 1a and b). Two effects contribute to this observation: (i) PiF-IR is surface sensitive and PMIS-C8 is expected to bind to the Au substrate through its thiol groups, while the alkyl chain forms the interface with air[29] facing the AFM tip, and (ii) PiF-IR is sensitive to field enhancement and the direction of force detection perpendicular to the sample stage[12,22,26] and the alkyl chains are flexible, performing CH$_3$ and CH$_2$ bend vibrations more freely in space in contrast to vibrations of the perylene core.[29] This mobility of the alkyl chain was not included in the calculation of polarization-resolved IR spectra presented in Fig. 1d–f, which show a stronger intensity of these bands in the direction parallel to the perylene core long axis (x-component). IR spectra were calculated using a lower energy confirmation of the molecular structure of PMIS-C8 (ref. 29) showing a strict and straight orientation of the alkyl chain (see inset in Fig. 1e). This is not necessarily the case on the surface of the PMIS-C8 monolayer films at room temperature, resulting in a decrease in the orientational anisotropy in these bands compared to the results of the calculation. The perylene core is less flexible in re-orientation within monolayer films.[29] The high spatial resolution of PiF-IR can resolve local intensity variations in bands related to perylene core vibrations (see Fig. 1a). The scan areas for the PiF-IR spectra shown in Fig. 1a and b are presented in the SI together with arrows marking the positions of spectral acquisition and two further investigated sample positions. We will use hyperspectral PiF-IR scans for studying correlations of spectral bands and sample positions because of their higher positional accuracy which is detailed in the methods section.

PiF-IR probes molecular orientation in PMIS-C8 monolayers on Au substrates

PIF contrasts acquired on PMIS-C8 monolayer films on nanostructured Au at illumination frequencies related to vibrations of the perylene core show local intensity modulations; an example is seen in Fig. 2a. The intensity variations

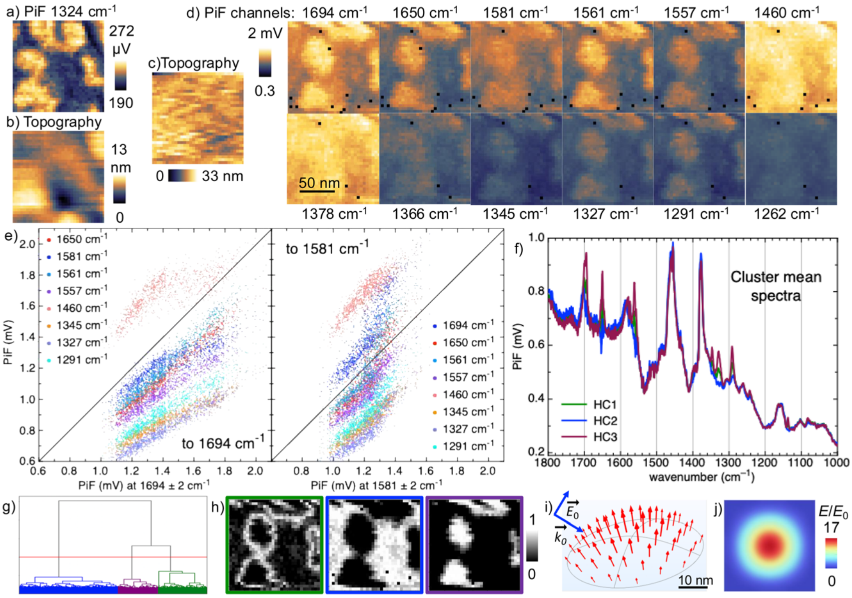

Fig. 2 Local molecular orientation of PMIS-C8 on a nanostructured Au substrate visualized using PiF-IR hyperspectral bands. (a) PiF and (b) simultaneously acquired topography in single frequency scan at $\nu = 1324\ \mathrm{cm}^{-1}$, (c) topography acquired with a PiF-IR hyperscan in the same area, (d) PiF contrast of selected bands in the hyperscan, (e) PiF intensity correlations of characteristic PMIS-C8 bands of the hyperscan to the bands at 1694 cm^{-1} (left) and 1581 cm^{-1} (right); (f–h) HCA analysis of hyperspectrum: (f) cluster mean spectra, (g) dendrogram and (h) factor maps in matching colors, (i and j) modeled photo-induced E-field on the Au nanostructure: (i) orientation and (j) normalized field strength in sample plane.

roughly match the sample topography in this position (Fig. 2b), which shows the typical surface structure of the evaporated Au layer of the underlying nanostructured Au substrate. We acquired a PiF-IR hyperscan in this area to study correlations between band intensities. As detailed in the methods section, the simultaneously acquired topography image (Fig. 2c) is rather noisy due to long acquisition, while the PIF channels (Fig. 2d) are less sensitive to instrument noise. The structure seen in the PiF channels, which are related to vibrations of the imide group (1694 and 1650 cm^{-1}) and the perylene core (1561, 1557, 1345, 1327 and 1291 cm^{-1}), follows the PiF contrast seen in the single frequency scan (Fig. 2a) of this sample position. The slight distortion of the structure between the two scans results from an accumulation of positional drift in the instrument over the long acquisition time of the hyperscan. In contrast, PiF channels connected with a substantial amount of CH_2 and CH_3 bend vibrations show less contrast, in particular those acquired at 1460 and 1378 cm^{-1}. The low intensity and low contrast in the channel at 1262 cm^{-1} confirms the absence of the frequent contaminant PDMS in this sample position.

A pixel-wise correlation of PiF-intensities in characteristic bands (Fig. 2e) provides further details of the correlations between the PMIS-C8 absorption bands. Below a certain threshold, ($\approx$1.4 mV for the channel at 1694 cm^{-1} and $\approx$1.2 mV for the channel at 1581 cm^{-1} in Fig. 2e left and right, respectively) all PiF-intensities show a parallel rise. Above this threshold, PiF intensities stay almost constant in the two channels at 1581 and 1460 cm^{-1}, while they continue to increase in parallel in the channels at 1694, 1650, 1561, 1557, 1345, 1327, and 1291 cm^{-1}. This correlation of vibrational bands with μ oriented along the molecular x and y-axes (see Table 1) shows that vibrations parallel to the perylene core's long axis cannot be discriminated from those parallel to its short axis. Seemingly, in positions related to PiF intensities above the threshold, the molecules orient mostly with its core perpendicular to the substrate, but without a definite orientation of their long axes. This interpretation is consistent with the formation of stacked PMIS-C8 dimers in monolayer LB films on Ag substrates.[29] Due to the twist in the perlene core caused by the large chlorine atoms in the bay positions, the stacks only form between half of the core.[29] As a consequence, there is a tilt angle between the molecular long axes and a turn between the imide group orientations, which can explain the correlation between intensities of molecular vibrations oriented parallel to the long and short axes of the perylene core.

Further insights on local molecular orientation can be derived from an HCA analysis of this hyperspectral scan (Fig. 2f–h). The cluster mean spectra (HC1, HC2 and HC3 in Fig. 2f) calculated for the selected clusters in the dendrogram (Fig. 2g) differ in the intensities of bands that are sensitive to molecular orientation (imide group vibrations at 1694 and 1650 cm^{-1} and perylene core vibrations at 1561, 1557, 1345, 1327 and 1291 cm^{-1}). Factor maps were derived from a linear combination of HC1, HC2 and HC3 in each pixel (for details, see the Methods section). They show a correlation of the relative intensities of the three components (presented in matching colors in Fig. 2h) with the sample topography: HC3 relates high intensities in the bands sensitive to molecular orientation (Fig. 2f) with elevated regions in the sample topography (compare Fig. 2b, c and h taking also into account the distortion of the scanned area during the hyperscan acquisition). In HC2 the orientation-sensitive bands show low intensities, suggesting an orientation of the perylene core mostly parallel to the sample surface. A high factor of HC2 correlates mainly with lower regions in the sample topography, which also show lower PiF intensities in hyperspectral channels related to imide and perylene core vibrations in Fig. 2d. A high factor of HC1 (Fig. 2g) marks the contour of elevated areas in the sample topography. HC1 shows intermediate intensities in the orientation sensitive spectral bands compared to the other two mean cluster spectra (Fig. 2f). Thus, its distribution can be assigned to regions in the sample where the perylene cores turn from an orientation perpendicular to the sample plane to an in-plane orientation. This interpretation is further supported by results from modeling the photo-induced field on a model nanostructure: the field vectors are oriented normal to the surface of the nanostructure while the field intensity shows a decrease from its top region to its edge; see Fig. 2i and j, respectively. For details of the optical modeling, we refer to the methods section and the SI. The hyperscan covers only a small sample area containing a few “hills” and “valleys” in the sample topography. We will investigate molecular orientation and field effects in more detail using single frequency scans covering a larger scan area in the next section after presenting results of a comparable hyperscan obtained from a PMIS-C8 monolayer on planar Au.

Planar Au substrates contain planar areas with only few nm height variation, which are surrounded by small steps and small particles, as can be seen in the AFM investigation of a 5 μm wide area presented in Fig. S2a in the SI. PMIS-C8 monolayers form a pattern of up to 100 nm wide planar flakes separated by small valleys and dips (see Fig. S3a and b). PiF contrasts at $\nu = 1324$ cm^{-1} and $\nu = 1694$ cm^{-1} show an increased intensity in the planar areas compared to the valleys; see overview scans in Fig. S4. We selected a 130 nm wide area for a PiF-IR hyperscan, which covered several planar areas and valleys from these overview scans; matching cuts of PiF contrast and topography from the scan at 1694 cm^{-1} are presented in Fig. 3a and b, respectively. The topography image (Fig. 3c) acquired simultaneously with the hyperscan is too noisy to discriminate its structure. Thus, we will again rely on the topography (Fig. 3b) of the previously acquired single frequency scan to relate PiF contrasts in selected channels of the hyperscan (Fig. 3d) with the sample topography. Similar to PMIS-C8 on nanostructured Au, we find an overall high intensity in the two bands assigned with CH_2 and CH_3 bend vibrations in the alkyl chain, while in the bands which are characteristic for molecular orientation, we see a much more pronounced intensity contrast in the corresponding PiF channels. In these bands, high PiF intensities are seen on planar areas, while the valleys show much lower PiF (Fig. 3d). The pixel-wise correlations of PiF contrasts in the selected channels confirm the different behavior of PiF intensities in the bands at 1581 and 1460 cm^{-1} from those related to molecular orientation (Fig. 3e). Thresholds cannot be discriminated, which may result from the strong contributions of residual water vapor absorption in the spectral region of 1800–1350 cm^{-1}, which can be seen in the cluster mean spectra of the HCA analysis in Fig. 3f. The three cluster mean spectra for the clusters selected from the dendrogram (Fig. 3g) again vary by their intensities in bands characteristic for perylene core vibrations: HC2 shows the highest intensities in the two bands at $\nu = 1327$ cm^{-1} and $\nu = 1291$ cm^{-1}, which are outside the spectral region influenced by water vapor absorption bands. The corresponding factor map (green) in Fig. 3h assigns this component to planar areas in the sample topography, while the cluster mean spectrum showing lowest intensities in the two bands (HC1) is assigned to the valleys (Fig. 3h, blue). Different to the HCA of

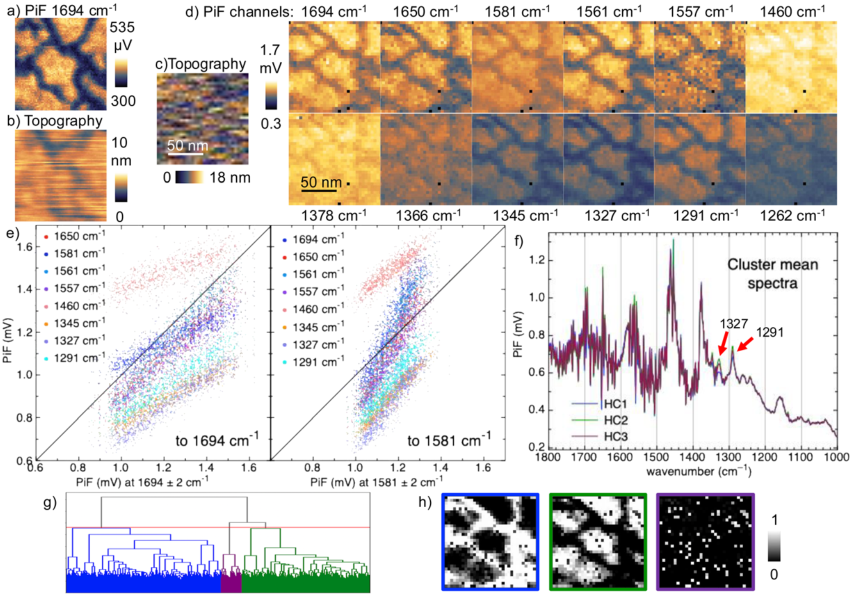

Fig. 3 Local molecular orientation of PMIS-C8 on the planar Au substrate visualized using PiF-IR hyperspectral bands. Selected areas of (a) PiF and (b) simultaneously acquired topography in single frequency scan at $\nu = 1694\ \text{cm}^{-1}$ shown in Fig. S5, (c) topography acquired with the PiF-IR hyperscan in the same area, (d) PiF contrast of selected bands in the hyperscan, (e) PiF intensity correlations of characteristic PMIS-C8 bands of the hyperscan to the bands at 1694 cm^{-1} (left) and 1581 cm^{-1} (right); (f–h) HCA analysis of the hyperspectrum: (f) cluster mean spectra with characteristic bands marked by red arrows, (g) dendrogram and (h) factor maps.

PMIS-C8 on nanostructured Au (Fig. 2f and g), the cluster mean spectrum showing intermediate PiF intensities in the two bands (HC3) is not assigned to a particular sample structure; high factors of HC3 appear distributed over the whole sample area (Fig. 3h, purple). However, the factor maps of the two other clusters show some overlaps in the contour regions. It seems that three clusters were not enough to find the spectra related to the contours of the planar areas, or it is not possible to discriminate this area using an HCA, which may be a result of the strong water vapor lines in this data set. We had acquired two succeeding single frequency scans on the same sample area at $\nu = 1650\ \text{cm}^{-1}$ and $\nu = 1694\ \text{cm}^{-1}$ at two positions of PMIS-C8 on planar Au substrates. We used them to compare local band intensities by cropping the areas and presenting combined images using RGB colors; see Fig. S6. However, the relative PiF intensity variation in the two sample areas does not show any distinct pattern. Thus, PMIS-C8 appears to align with its perylene core perpendicular to the planar sample surface, while vibrations parallel to the short and long axes of the perylene core cannot be discriminated in the monolayer films, in agreement with the observed dimer formation on Ag substrates.[29]

On nanostructured Au substrates, PMIS-C8 generally does not orient with its perylene core perpendicular to the Au surface, as can be seen from scans of larger areas presented in Fig. 4. The PiF contrast acquired in a 1 µm wide area at $\nu =$

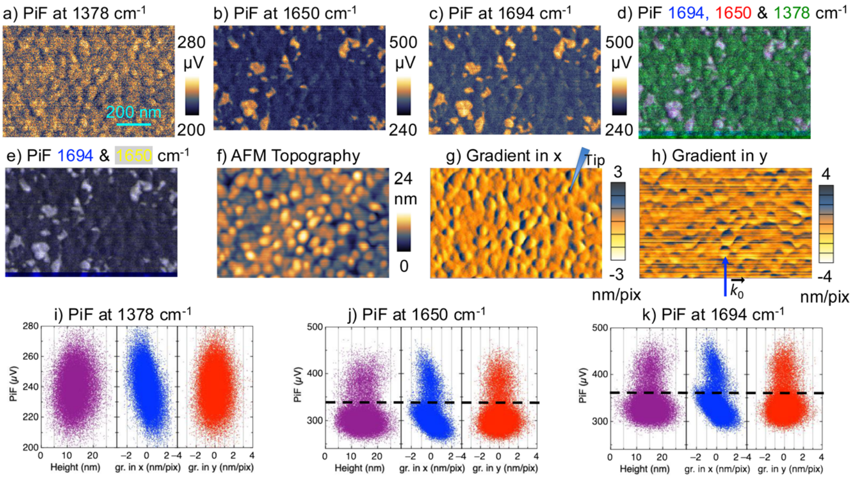

Fig. 4 Molecular orientation of PMIS-C8 compared to field effects in the PMIS-C8 monolayer on nanostructured Au: (a–c) PiF contrasts of a 1 µm wide area acquired at $\nu = 1378\ \text{cm}^{-1}$, $\nu = 1650\ \text{cm}^{-1}$ and $\nu = 1694\ \text{cm}^{-1}$, respectively; (d and e) RGB images of cropped areas of PiF contrasts at (d) 1694 cm^{-1} (B), 1650 cm^{-1} (R) and 1378 cm^{-1} (G), and (e) 1694 cm^{-1} (B) and 1650 cm^{-1} (R + G = yellow); (f) AFM topography and (g and h) gradients of topography calculated in the (g) horizontal (x) and (h) vertical (y) direction. The blue shape in (g) depicts the inclination of the scanning AFM tip. The blue arrow in (h) marks the propagation k_0 of the incident field E_0. (i–k) Correlation plots of PiF intensities in the three frequencies with sample topography and gradients; dashed lines in (j and k) mark the separation between subpopulations with high and low PiF intensities corresponding to $\mu \parallel E$ and $\mu \nparallel E$, respectively.

1378 cm^{-1} (Fig. 4a) reveals a complete coverage of the area by PMIS-C8 showing only moderate intensity variations related to the film surface structure (Fig. 4a). Subsequently acquired PiF contrasts at $\nu = 1650\ \text{cm}^{-1}$ (Fig. 4b) and $\nu = 1694\ \text{cm}^{-1}$ (Fig. 4c) show varying intensities in these two absorption bands of the imide group with μ oriented parallel to the perylene core. A high PiF signal is visible only in several areas of this sample position extending over less than 100 nm. From this we conclude that the PMIS-C8 molecules generally orient with their perylene core parallel to the sample plane. The irregular surface structure and curvature of the evaporated Au substrate seem to prevent a large scale organization of PMIS-C8 in its preferred orientation perpendicular to the Au substrate, which has been found on planar Au (Fig. 3).

Field coupling effects

To evaluate possible coupling effects of the film structure with the local photo-induced field, we derived gradients of the unprocessed sample topography (Fig. 4f) in horizontal (x) and vertical (y) directions; see Fig. 4g and h, respectively. Pixel-wise correlations of PiF intensities in the three frequencies with sample heights confirm the observation seen in the PiF contrasts of the scanned areas: for $\nu = 1378\ \text{cm}^{-1}$ a broad and unspecific distribution of PiF intensities is found. In the orientation-sensitive bands at 1650 and 1694 cm^{-1}, two subpopulations become visible: (i) large subpopulations showing low PiF intensities are seen below the dashed lines in Fig. 4j and k. They cover the full range of heights in the sample topography and correspond to positions with $\mu \nparallel E$; and (ii) smaller subpopulations showing higher PiF intensities appear above these dashed lines. The higher PiF intensities are mostly limited to height values in a narrower range around the mean heights (Fig. 4j and k). These subpopulations contain positions corresponding to $\mu \parallel E$.

In all three frequencies, PiF intensities increase with decreasing gradients in the horizontal direction (x). In the orientation-sensitive bands, the two subpopulations below and above the dashed lines in Fig. 4j and k increase separately. This general correlation between PiF intensities and gradients along x is observed independent of the particular orientation of μ with respect to the orientation of E for all three studied frequencies. It is caused by the hybrid field coupling with the probing AFM tip, as will be explained in the following: negative gradients are assigned to the right hand slope of the "hill" structures. According to the manufacturer, the NCH-ppp tips used for scanning the samples, exhibit a tilt to the right, as depicted in Fig. 4g. The effect of this tip tilt on nanostructured surfaces was demonstrated by Anindo *et al.*, who combined modeling and experiment to investigate the hybrid field coupling of the incident electric field E_0 with such a Pt-coated tip and a polymer nanosphere.[12] The observed correlation between PiF intensities and gradients for the PMIS-C8 monolayer on nanostructured Au is consistent with the reported increase of PiF intensities and modeled field E at the right side of the nanosphere. An additional influence of the direction of the incident field E_0 from the bottom line of the scan (blue arrow in Fig. 4h) cannot be discerned. In the slow scanning direction, PiF intensities seem to be distributed symmetrically with positive and negative gradients. However, this influence might be concealed by noise in topography acquisition along the slow scanning direction, which is the cause of the horizontal lines seen in the gradient image in Fig. 4h.

Discussion

From theoretical investigation combined with modeling it is known that the plasmonic/hybrid field enhancement between a metal tip and a metal/polymer film surface or nanostructure can reach several orders of magnitude, when polarized in the plane of incidence (p-polarization) and is much weaker for s-polarization.[7,12,55] Theoretical considerations by Pascual Robledo *et al.* show that in thin layers on highly reflecting surfaces the sensitivity to probe in-plane vibrations is reduced compared to probing out-of plane vibrations due to a vertical orientation of the near-field.[55] Our PiF-IR investigation of oriented PMIS-C8 monolayer films on Au substrates provides an experimental evaluation of the modeled results by comparing PiF intensities in orientation sensitive bands related to vibrations of the perylene core[50] and the imide group[50] with PiF intensities of orientation-insensitive bands related to CH_3 and CH_2 bending[52] in the alkyl chain.

As expected, our PiF-IR results are able to reveal the orientation of PMIS-C8 with its perylene core perpendicular to the sample plane and the alkyl chain facing the air interface in LB monolayer films on planar Au substrate regions, and to some extent also on evaporated Au nanostructures. This observation agrees with a literature report on the macromolecular orientation of PMIS-C8 in LB films on plasmonically active Ag island substrates investigated using surface-enhanced resonance Raman spectroscopy (SERRS).[29] Due to the high lateral resolution of PiF-IR (≤5 nm),[10] we could additionally resolve the lateral structure of the PMIS-C8 films on both types of Au substrates on an almost single-molecule scale. From this, we found a reduced signal of characteristic bands related to vibrations of the perylene core in shallow 10–20 nm wide valleys between planar Au regions, which were present on our planar Au substrates. In contrast, the PiF signal in bands related to the arbitrarily oriented alkyl chain showed only small intensity variations between the planar surface and valleys. On nanostructured Au substrates, we found variations in how PMIS-C8 was oriented on top of the Au islands formed during the evaporation of Au onto SiO_2 substrates: on top of some of these "hills" a high PiF signal in the characteristic bands associated with the imide group and core vibrations indicate an orientation of the molecules with their perylene core perpendicular to the substrate, similar to the observation on planar Au. However, regions showing this molecular orientation did not extend over more than 3–4 neighboring islands. In most of the film, the characteristic bands associated with perylene core and imide group vibrations were absent or reduced. The cause of the varying molecular orientation on top of the nanostructured Au is not clear. A limiting factor on molecular alignment resulting from the curvature of the Au surface may have some influence.

Our PiF-IR hyperspectral analysis of a region in the PMIS-C8 monolayer on nanostructured Au which showed high PiF intensities in the orientation-sensitive bands provides further insights into the local PMIS-C8 orientation in combination with field enhancement and orientation. For PiF channels related to isotropically oriented CH_3 and CH_2 bending of the alkyl chain ($\nu = 1378$ and 1460 cm^{-1}), we found enhanced PiF intensities on top of the "hills" in the nanostructure and a decrease with decreasing height of the topography. This observation agrees with the distribution of the photoinduced field intensities, which we obtained on a modeled nanostructure resembling one of the Au islands using finite element modeling (FEM). Applying a hierarchical cluster analysis, we found three distinctive subsets in the hyperscan: (i) in the top regions of the nanostructures, high PiF-intensities are seen in the orientation-sensitive bands. This agrees with the field enhancement observed also in the isotropic bands in combination with a molecular orientation of PMIS-C8 with its perylene core perpendicular to the Au surface; (ii) in the shallow regions of the sample, PiF spectra showed low absorption or absence of absorption in the orientation-sensitive bands while the intensity in the two prominent bands related to isotropically oriented alkyl chain vibrations ($\nu = 1378$ and 1460 cm^{-1}) was not altered, which clearly shows that the perylene cores were oriented rather parallel to the Au surface and not perpendicular to it in that region; and (iii) intermediate PiF intensities were found in the orientation-sensitive bands in the contours of the islands. According to the theoretical considerations by Pascual Robledo *et al.*, also lateral field components are present at the apex of the metal tip.[55] The field orientation on top of our modeled nanostructure is aligned perpendicular to the surface of the structure. Although our simplified model did not include any AFM tip, we assume that the coupled field between the tip and the nanostructure also contains a considerable component perpendicular to the surface of the nanostructure due to the lateral components present in the field close to the tip apex. Thus, we would expect to see also high PiF in the orientation-sensitive bands of

PMIS-C8 in the case that the perylene core was oriented perpendicular to the substrate surface in this region. Since this is not the case, we conclude that the reduced PiF intensities are caused by a molecular tilt in respect to the surface normal.

To study field coupling effects of the incident field with the nanostructure and between nanostructure and tip, we correlated PiF intensities obtained in three bands from PMIS-C8 on a 1 μm wide area with gradients of the local topography. PiF intensities in both anisotropically-oriented imide vibration bands as well as at $\nu = 1378\ \text{cm}^{-1}$ (isotropically oriented CH_3 and CH_2 bending of the alkyl chain) showed an increase with increasing gradients from left to right in the horizontal fast scanning (x) direction. The scanning AFM tip is inclined by $\approx 30°$ from the right. We assign the observed asymmetry to an effect of field coupling between the inclined tip and the Au nanostructures enhancing the absorption in the thin PMIS-C8 layer on the nanostructure, which is consistent with an experimentally observed signal enhancement on a polymer nanosphere.[12] In the vertical slow scanning (y) direction no asymmetry of PiF intensities with respect to the gradient could be discerned. However, the slow scanning direction is much more influenced by noise. We therefore suggest further experiments with a varied fast scanning direction to investigate a mutual influence of field coupling also parallel to the field propagation vector k_0 of the incident field E_0.

Conclusions

We used the high precision of PiF-IR to study local anisotropies in detected signals of an anisotropically absorbing LB monolayer on planar and nanostructured Au substrates. Our results show a strong signal obtained from out-of plane vibrations on highly reflecting planar Au substrates, confirming theoretical considerations by Pascual Robledo *et al.*[55] By comparing PiF intensities obtained from isotropically absorbing CH_3 and CH_2 bending vibrations of the alkyl chain with those related to orientation-sensitive molecular absorptions, we were able to discriminate between effects caused by molecular orientation and those caused by coupling of the photo-induced field on nanostructured Au surfaces. By correlating PiF intensities in isotropically and anisotropically absorbing molecular vibration bands with gradients of the local topography we found an increase of intensities in the direction of the inclination angle of the scanning AFM tip in agreement with experimental observations of PiF intensities on a polymer sphere combined with modeling by Anindo *et al.*[12]

Our results demonstrate the potential of PiF-IR to investigate local anisotropies on nanostructured surfaces and contribute to their understanding. The enhanced understanding will improve the interpretation of results obtained using nanoscale infrared spectroscopic imaging methods and enable their application to a wider area of nanostructured materials.

Author contributions

Ayona James: experimental, data analysis, writing. Maryam Ali: experimental, data analysis, programming, supervision. Zekai Ye: experimental, supervision, writing. Phan Thi Yen Nhi: computation, data analysis, writing. Sharon Xavi: modeling, writing. Mashiat Huq: modeling. Sajib Barua: experimental. Yisak

Tsegazab: experimental. Anna Elmanova: computation. Robin Schneider: experimental, data analysis. Olga Usitmenko: experimental, data analysis. Sarmiza-Elena Stanca: experimental. Marco Diegel: experimental. Andrea Dellith: experimental, data analysis. Uwe Hübner: experimental, methodology. Christoph Krafft: experimental. Jasmin Finkelmeyer: experimental, methodology. Maximilian Hupfer: experimental, methodology. Kalina Peneva: conceptualization, supervision, project administration, funding acquisition. Matthias Zeisberger: conceptualization, modeling, methodology. Christin David: modeling, methodology, supervision, writing. Martin Presselt: conceptualization, methodology, computation, supervision, writing. Daniela Täuber: conceptualization, writing, methodology, experimental, data analysis, supervision, project administration, funding acquisition.

Conflicts of interest

There are no conflicts to declare.

Data availability

Data for this article,[54] including PiF-IR single frequency scans, spectra & hyperspectra, complementary FTIR & ATR spectra, AFM height & phase data, a BAM series and interactive calculated IR spectra are available at zenodo: https://doi.org/10.5281/zenodo.18060233.

The code for hyPIRana[35] can be found on zenodo with DOI: https://doi.org/10.5281/zenodo.15270456. The code used for this study is also available as release v2.1.0 of our home-built software code hyPIRana on github: https://github.com/BioPOLIM/hyPIRana.

Supplementary information (SI): (i) exemplary BAM images of a PMIS-C8 film formed at the water surface before film deposition, (ii) AFM results of pristine substrates and PMIS-C8 monolayer films, (iii) topography images and PiF-contrasts of PiF-IR scan areas of the spectra presented in the main text together with two additional series of spectra on different sample positions, (iv) further PiF contrasts of PMIS-C8 monolayers on planar Au, and (v) further details on COMSOL modeling. See DOI: https://doi.org/10.1039/d6fd00003g.

Acknowledgements

For the VistaScope and the MirCat QCL financial support of the European Union *via* the Europäischer Fonds für Regionale Entwicklung (EFRE) and the Thüringer Ministerium für Wirtschaft, Wissenschaft und Digitale Gesellschaft (TMWWDG) is acknowledged (Projects: 2018 FGI 0023 and 2023 FGI 0018). DT acknowledges funding by a postdoctoral Scholarship (PolIRim) from Friedrich Schiller University Jena in 2020. DT and MA acknowledge funding from the German Research Foundation (DFG, Project: 542825796 "HiResi4RPE"). KP and OU acknowledge funding from DFG (CRC 1375 NOA, project number 398816777, Project B5). KP acknowledges funding from DFG in the framework of FOR5301 "FuncHeal" (project number 455748945, projects P3). The authors thank Beate Truckenbrodt and Ines Hirsch for providing access to the KSV NIMA Langmuir–Blodgett trough

in their education lab at the institute of Physical Chemistry, FSU Jena, when the otherwise used KSV 5000 was not available for LB film deposition.

Notes and references

1 J. J. Schwartz, S. D. Jakob and A. Centrone, *Chem. Soc. Rev.*, 2022, **51**, 5248–5267.
2 Q. Xie and X. G. Xu, *Langmuir*, 2023, 17593–17599.
3 J. Shen, B.-I. Noh, P. Chen and S. Dai, *Small Sci.*, 2024, **4**, 2400297.
4 C. Höppener, J. Aizpurua, H. Chen, S. Gräfe, A. Jorio, S. Kupfer, Z. Zhang and V. Deckert, *Nat. Rev. Methods Primers*, 2024, **4**, 1–20.
5 M. Ali, R. Schneider, A. Strecker, N. Krishnakumar, S. Unger, M. Soltaninezhad, J. Kirchhoff, A. Tannert, K. A. Dragounova, R. Heintzmann, A.-D. Müller, C. Krafft, U. Neugebauer and D. Täuber, *Anal. Chem.*, 2025, **97**, 23914–23926.
6 J. Waeytens, J. Mathurin, A. Deniset-Besseau, V. Arluison, L. Bousset, H. Rezaei, V. Raussens and A. Dazzi, *Analyst*, 2021, **146**, 132–145.
7 J. Jahng, B. Kim and E. S. Lee, *Phys. Rev. B: Condens. Matter Mater. Phys.*, 2022, **106**, 155424.
8 G. Bakir, B. E. Girouard, R. Wiens, S. Mastel, E. Dillon, M. Kansiz and K. M. Gough, *Molecules*, 2020, **25**, 4295.
9 X. Luo, Y. Xue, J. Wu, W. Cai, D. Täuber, I. Malovicho, B. Sava, C. Cen, X. Lu, C. Zhao, I. G. Scheblykin, J. Yu, W. Mai, F. Lui, E. Wang and L. Hou, *Appl. Phys. Lett.*, 2022, **121**(23), 233301, DOI: 10.1063/5.0128850.
10 M. R. Shcherbakov, E. O. Potma, Y. Sugawara, D. Nowak, M. Stepanova, P. R. Davies, J. Davies-Jones and H. K. Wickramasinghe, *Nat. Rev. Methods Primers*, 2025, **5**, 34.
11 Q. Xie, H. Wang and X. G. Xu, *J. Phys. Chem. C*, 2022, **126**, 8393–8399.
12 S. T. Anindo, D. Täuber and C. David, *J. Phys. Chem. C*, 2025, **129**, 4517–4529.
13 P. R. Griffiths, *Spectroscopic Properties of Inorganic and Organometallic Compounds*, 2013, vol. 44, pp. 95–122.
14 K. Ataka and J. Heberle, *Anal. Bioanal. Chem.*, 2007, **388**, 47–54.
15 X. G. Xu, M. Rang, I. M. Craig and M. B. Raschke, *J. Phys. Chem. Lett.*, 2012, **3**, 1836–1841.
16 F. Huth, A. Chuvilin, M. Schnell, I. Amenabar, R. Krutokhvostov, S. Lopatin and R. Hillenbrand, *Nano Lett.*, 2013, **13**, 1065–1072.
17 A. Dazzi, C. B. Prater, Q. Hu, D. B. Chase, J. F. Rabolt and C. Marcott, *Appl. Spectrosc.*, 2012, **66**, 1365–1384.
18 F. Lu, M. Jin and M. A. Belkin, *Nat. Protoc.*, 2014, **8**, 307–312.
19 J. Mathurin, A. Deniset-Besseau and A. Dazzi, *Acta Phys. Pol., A*, 2020, **137**, 29–32.
20 N. Hondl, L. Neubauer, V. Ramos-Garcia, J. Kuligowski, M. Bishara, E. Sevcsik, B. Lendl and G. Ramer, *ACS Meas. Sci. Au*, 2025, **5**, 469–476.
21 J. Jahng, E. O. Potma and E. S. Lee, *Anal. Chem.*, 2018, **90**, 11054–11061.
22 A. A. Sifat, J. Jahng and E. O. Potma, *Chem. Soc. Rev.*, 2022, **51**, 4208–4222.
23 J. Joseph, L. Spantzel, M. Ali, D. Moonnukandathil Joseph, S. Unger, K. Reglinski, C. Krafft, A.-D. Müller, C. Eggeling, R. Heintzmann, M. Börsch, A. T. Press and D. Täuber, *Spectrochim. Acta, Part A*, 2024, **306**, 123612.

24 R. A. Murdick, W. Morrison, D. Nowak, T. R. Albrecht, J. Jahng and S. Park, *Jpn. J. Appl. Phys.*, 2017, **56**, 08LA04.

25 M. W. Förster, L. M. Otter, J. J. Brocks, K. Jayasoma, D. Cisneros-Lazaro, D. Nowak, J. Stolarski and B. Knowles, *Geostand. Geoanal. Res.*, 2025, **49**, 685–703.

26 J. Jahng, E. O. Potma and E. S. Lee, *Proc. Natl. Acad. Sci. U. S. A.*, 2019, **116**, 26359–26366.

27 D. Täuber, A. Dobrovolsky, R. Camacho and I. G. Scheblykin, *Nano Lett.*, 2016, **16**, 5087–5094.

28 Y. T. Gerase, J. Garcia Lopez, J. P. Madalaimuthu, A. Elmanova, S. J. Finkelmeyer, A. Dellith, D. Blaschke, H. Schmidt, K. Peneva, H. Hoppe and M. Presselt, *ACS Appl. Electron. Mater.*, 2024, **6**, 2258–2267.

29 M. L. Hupfer, R. Meyer, T. Deckert-Gaudig, S. Ghosh, A. Skabeev, K. Peneva, V. Deckert, B. Dietzek and M. Presselt, *Langmuir*, 2021, **37**, 11018–11026.

30 H. Abul-Futouh, A. Skabeev, D. Botteri, Y. Zagranyarski, H. Görls, W. Weigand and K. Peneva, *Organometallics*, 2018, **37**, 3278–3285.

31 S. Das, J. Preiss, J. Plentz, U. Bruckner, M. von der Luhe, O. Eckardt, A. Dathe, F. H. Schacher, E. Tauscher, U. Ritter, A. Csaki, G. Andra, B. Dietzek and M. Presselt, *Adv. Energy Mater.*, 2018, **8**, 1801737.

32 M. L. Hupfer, M. Kaufmann, L. Roussille, J. Preiss, D. Weiss, K. Hinrichs, V. Deckert, B. Dietzek, R. Beckert and M. Presselt, *Langmuir*, 2019, **35**, 2561–2570.

33 M. L. Hupfer, M. Kaufmann, F. Herrmann-Westendorf, T. Sachse, L. Roussille, K. H. Feller, D. Weiss, V. Deckert, R. Beckert, B. Dietzek and M. Presselt, *ACS Appl. Mater. Interfaces*, 2017, **9**, 44181–44191.

34 D. Nečas and P. Klapetek, *Open Phys.*, 2012, **10**, 181–188.

35 M. Ali, S. Unger and D. Täuber, hyPIRana v2.1.0 – Analysis code for combined analysis of hyperspectral data in mid-IR photo-induced force microscopy (PiF-IR), 2026, https://zenodo.org/records/15270456.

36 I. S. Ufimtsev and T. J. Martinez, *J. Chem. Theory Comput.*, 2009, **5**, 2619–2628.

37 C. M. Isborn, N. Luehr, I. S. Ufimtsev and T. J. Martínez, *J. Chem. Theory Comput.*, 2011, **7**, 1814–1823.

38 A. V. Titov, I. S. Ufimtsev, N. Luehr and T. J. Martinez, *J. Chem. Theory Comput.*, 2013, **9**, 213–221.

39 C. Song, L.-P. Wang and T. J. Martínez, *J. Chem. Theory Comput.*, 2016, **12**, 92–106.

40 W. Beenken, W. Maes, M. Kruk, T. Martínez and M. Presselt, *J. Phys. Chem. A*, 2015, **119**, 6875–6883.

41 C. Song, L.-P. Wang, T. Sachse, J. Preiß, M. Presselt and T. J. Martínez, *J. Chem. Phys.*, 2015, **143**, 014114.

42 M. Presselt, C. Schnedermann, M. Schmitt and J. Popp, *J. Phys. Chem. A*, 2009, **113**, 3210–3222.

43 S. Grimme, J. Antony, S. Ehrlich and H. Krieg, *J. Chem. Phys.*, 2010, **132**, 154104.

44 S. Das, J. Fiedler, O. Stauffert, M. Walter, S. Y. Buhmann and M. Presselt, *Phys. Chem. Chem. Phys.*, 2020, **22**, 23295–23306.

45 T. Yanai, D. P. Tew and N. C. Handy, *Chem. Phys. Lett.*, 2004, **393**, 51–57.

46 A. Schäfer, H. Horn and R. Ahlrichs, *J. Chem. Phys.*, 1992, **97**, 2571–2577.

47 K. Seshadri, P. Liu and D. R. Koes, *J. Chem. Educ.*, 2020, **97**, 3872–3876.

48 R. L. Olmon, B. Slovick, T. W. Johnson, D. Shelton, S.-H. Oh, G. D. Boreman and M. B. Raschke, *Phys. Rev. B: Condens. Matter Mater. Phys.*, 2012, **86**, 235147.

49 D. Franta, D. Nečas, I. Ohlídal and A. Giglia, *Optical Micro-and Nanometrology VI*, 2016, pp. 253–267.

50 T. Del Caño, V. Parra, M. L. Rodríguez-Méndez, R. Aroca and J. A. De Saja, *Org. Electron.*, 2004, **5**, 107–114.

51 A. Łapiński, A. Graja, I. Olejniczak, A. Bogucki, M. Połomska, J. Baffreau, L. Perrin, S. Leroy-Lhez and P. Hudhomme, *Molecular Crystals and Liquid Crystals*, 2006, vol. 447, pp. 87/[405]–103/[421].

52 J. Coates, in *Encyclopedia of Analytical Chemistry*, John Wiley & Sons, Ltd, Chichester, UK, 2006, pp. 10815–10837.

53 M. L. Hupfer, D. Blaschke, H. Schmidt and M. Presselt, *Langmuir*, 2021, **37**, 13255–13264.

54 A. James, M. Ali, Z. Ye, R. Schneider, S. E. Stanca, C. Krafft, M. Diegel, A. Dellith, T. Y. N. Phan, A. Elmanova, M. Presselt and D. Täuber, PiF-IR data of PMIS-C8 monolayer films on nanostructured and planar Au substrates, complementary AFM, FTIR/ATR and BAM data and calculated PMIS-C8 spectra, 2025, https://zenodo.org/records/18060234.

55 I. Pascual Robledo, C. Maciel-Escudero, M. Schnell, L. Mester, J. Aizpurua and R. Hillenbrand, *ACS Photonics*, 2025, **12**, 3782–3793.